Archives of Computational Methods in Engineering manuscript No.
(will be inserted by the editor)

A comparative study of mixed resolved-unresolved CFD-DEM and unresolved CFD-DEM methods for the solution of particle-laden liquid flows

Sahan T.W. Kuruneru · Ewen Marechal · Michael Deligant · Sofiane Khelladi · Florent Ravelet · Suvash Saha · Emilie Sauret · Yuantong Gu.

Received: date / Accepted: date

Abstract The exorbitant economic and environmental cost associated with fouling propels the need to develop advanced numerical methods to accurately decipher the underlying phenomena of fouling and multiphase fluid transport in jet-engine fuel systems. Clogging of jet-fuel systems results in the foulants to settle in seconds to form a porous layer which restricts fuel flow. The objective of this research is to numerically examine the transient evolution of particle-laden liquid flow and particle accumulation on an idealized jet-fuel filter. This is achieved by using two numerical approaches: coupled unresolved computational fluid dynamics-discrete element method (CFD-DEM), and coupled mixed resolved-unresolved CFD-DEM method. We assess the efficacy of both numerical methods by comparing the numerical results against experimental data. Results have shown that the particle accumulation and deposition profiles are in good agreement with the experimental results. Moreover, it is found that the particle distribution spread along the length and height of the channel reflects the actual particle spread as observed in the experiments. The unresolved CFD-DEM and mixed resolved-resolved CFD-DEM method could be harnessed to study complex multiphase fluid flow transport in various other applications such as compact heat exchangers and fluidized beds.

Keywords Multiphase flow · particle-laden liquid flow · CFD-DEM · Brinkman penalization · fouling.

S.T.W. Kuruneru · E. Sauret · Y.T. Gu
Laboratory for Advanced Modelling and Simulation in Engineering and Science, School of Chemistry, Physics & Mechanical Engineering, Queensland University of Technology, Brisbane, Queensland,4011, Australia
E-mail: emilie.sauret@qut.edu.au; sahantw@gmail.com

S.C. Saha
School of Mechanical and Mechatronic Engineering, Faculty of Engineering and Information Technology, University of Sydney, Ultimo, New South Wales, 2007, Australia

E. Marechal, M. Deligant, S. Khelladi, F. Ravelet
Arts et Métiers ParisTech,Laboratoire de Dynamique des Fluides, DynFluid Lab - EA92, 151 Boulevard de l'Hopital, 75013 Paris, France E-mail: michael.deligant@ensam.eu

1 Introduction

Fouling is omnipresent in a myriad of industries such as automotive, aerospace, oil and gas, desalination, food processing, and building services [34, 35]. The overarching challenge facing engineers is the alleviation of fouling in heat exchangers. The economic penalties incurred due to heat exchanger fouling account for about 0.25 % of the GDP of industrialized nations [35]. Moreover, fouling has a profound impact on the economy such as reduction in productivity and increase in operational downtime. Fouling also has a negative impact on the global environment; approximately 2.5 % of global Carbon Dioxide emissions are attributable to fouling [34]. Moreover, fouling is responsible for higher maintenance costs, production losses, increased consumption of water, electricity, and increased safety hazards during operation and cleaning [34].

Fuel systems of turbojets comprise various hydraulic elements such as centrifugal and volumetric pumps, heat exchanger inlet screens, filters, valves, and other pressure of flow control members. Clogging and periodic accumulation of foulants, in the form of ice crystals, in a fuel-oil heat exchanger (FOHE) of an aircraft jet engine, can compromise aircraft performance [47]. In the event of "snow showers" which connotes the clogging of a jet-fuel filter, ice particles settle in seconds to form a porous layer, as shown in Figure 1. Ultimately, this severely restricts and hampers the flow of fuel. Snow

showers or fouling of filters of jet-fuel systems involves three distinct phases [30, 47, 45, 36, 3]. The first phase involves ice accretion comprising the growth of ice crystals from the water dissolved in the fuel and deposit of supercooled droplets. Secondly, this accumulated snow is released which occurs when the fuel velocity increases to 0.7 m/s to 0.8 m/s. This ice shedding process is the results of the shear stress caused by the amplification of drag. The release of accumulated ice particles laden with fuel will propagate into the jet-engine fuel system. The final phase involves clogging where this accumualted snow is carried by the fuel into the jet-engine fuel evidently choking fuel systems components instantly. This signifies the thermal transfer between the fuel system of the aircraft and the external environment which promotes icing conditions when the temperature of the fuel ratio, or that of the internal walls of the pipes, become less than 0 °C. Multiphase solid-liquid flows and particle accumulation on a filter is not well documented and poorly understood.

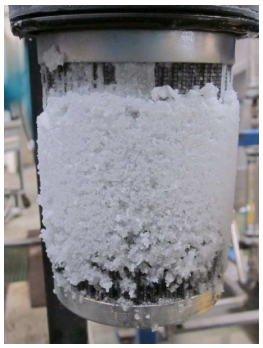

Fig. 1 Clogging of a typical fuel filter [32]

Ice crystals in fuel clogged the Rolls-Royce fuel-oil heat exchanger (FOHE) of each engine of British Airways flight 83 in 2008 [47]. This lead to the crash of this Boeing 777 jet just short of the runway at London Heathrow airport. The major challenge facing the aviation industry is the transport and the very rapid accumulation of dense flows of ice particles in sensitive equipment. Aviation safety authorities stipulate that fuel systems must be designed to ensure that the separation of water from jet fuel does not cause the engines to malfunction [2]. The US Deparment of Energy (DOE) stated that the economic penalty incurred due to fouling in refineries is found to be in excess of $2 billion per year [1]. The development of advanced numerical methods to study the dynamics of particulate deposit transport and accumulation is of paramount importance, and advances in the understanding and characterization of this phenomenon will lead to improved design of heat exchanger systems.

Various computational techniques have been developed to investigate the efficacy of heat exchangers. Ramagadia et al. [43] used finite volume method (FVM) together with a momentum interpolation method to investigate heat transfer characteristics of wavy channel (i.e. sinusoidal or arc-shaped walls) heat exchangers. Wavy channels are steadily gaining attention thanks to their manufacturing simplicity and potentially high energy savings and less power consumption. It was found that wavy-type heat exchangers exhibit higher heat transfer rates compared with straight channels due to the unsteady vortex shedding in the former device. Wang et al. [54] used a discrete phase model (DPM) coupled with a RNG k-ε turbulence model to investigate the real-time fouling characteristics of a H-type finned tube for waste heat recovery applications. It was found that fouling mainly occurs in the flow stagnation region specific regions such as in front of the tube and fins. The asymptotic fouling resistance decreases with increasing superficial inlet velocity, and fouling without removal increases linearly with time. However, the DPM model did not include fullly resolved particle-particle and particle-fluid interactions which must be enabled in dense particle-fluid flows to capture the complete dynamics of multiphase flows. Moreover, the morphology variation caused by the foulants on the finned tubes was not considered. Bayomy et al. [5] studied the optimum design of an aluminium foam computer heat sink by taking into account the highest heat transfer and lowest pumping power. One of the main findings was that as the Reynolds number increases, the thermal entry length amplifies. Additionally, the fully developed region, the Reynolds number plays a pertinent role in the local Nusselt number. De Bellis & Catalano [9] used Reynolds averaged Navier Stokes equations (RANS) together with SIMPLEX and non-dominated sorting genetic algorithm II to maximize the heat transfer of an immersed particle based heat exchanger. Pierre et al. [40] developed an optimal weak-variational formulation in the form of a spectral method (i.e. generalized Graetz problem) for the numerical analysis of the temperature fields and effectiveness of parallel convective heat exchangers. In the case of a two inlet/outlet semi-infinite counter-current tubes, it was found that the heat exchanger effectivess saturates with the exchanger length and Péclet number. The final effectiveness is controlled by the thermal conditions though the dependence on the imposed hydrodynamics is diminutive. Gu et al. [19] stated that the exclusion of the effects of the variability of air properties on the thermal-hydraulic charac-

teristics of heat exchangers for aero-engine cooling can overestimate the heat transfer and pressure drop.

The major limitation of the cited publications is that the evaluation of heat exchanger performance is based on several assumptions which make a systematic comprehension of complex multiphase transport and particulate fouling phenomena impossible. Firstly, the above cited publications that assess a heat exchanger's efficacy with the use of the Eulerian-Lagrangian or even with the use of CFD-DPM are neglecting fully resolved particle-particle interactions (i.e. zero particle volume) and neglecting the influence of the dispersed phase on the fluid continuum, and vice versa; which is incorrect considering the fact that heat exchangers in the chemical, oil & gas, and energy generation industries consist of dense multiphase (i.e. solid-liquid or solid-gas) flows [25]. Secondly, studies assume the system comprises single-phase flow which is not the norm in a myriad of engineering applications such as air-cooled heat exchangers [25, 49], or even fuel systems in turbojets [30]. Therefore, the development of robust numerical models is of paramount significance to decipher the mechanisms that govern multiphase transport and fouling in various engineering systems.

1.1 Numerical methods for particle-laden fluid flows

Studies have delved into the physics of multiphase transport using various advanced numerical techniques, each one having its own strengths and weaknesses. The standard Lagrangian based DPM (Discrete Phase Model) is similar to the Discrete Element Method (DEM) but the former neglects inter-particle collisions (i.e. zero particle volume); moreover, the DPM method neglects gas displacement by the particles. As such, the DPM is suited for dilute particulate suspensions [21] where a larger time-step could be used to reduce computational effort [33]. The Multiphase Particle-in-Cell (MPPIC) method is similar to the DEM methodology but particle movement and interactions are viewed statistically whilst excluding particle-particle and particle-wall interactions. The MPPIC method could also be deployed in dense solutions as it is impractical to use DEM method to simulate tens of thousands or millions of discrete particles. The Eulerian-Eulerian (i.e. two fluid model) method is not suitable to model dense (non-dilute) particle-fluid flows as the method treats both phases as an interpenetrating continua; moreover, the constitutive relations for solid particles and interphase interactions are generally not available [59]. Monte-Carlo methods do not permit one to accurately resolve all particle-fluid interactions particle micromechanics; moreover, the visualization of particle accumulation is not achievable. Population balance approaches, which is originally based on the Smoluchowski equation, is found to provide accurate predictions of particle aggregate size distribution; the drawback of this method is that predicting or obtaining the actual micromechanics and microstructure of the aggregation phenomena and particle aggregate interactions with fluid cannot be achieved [32]. The Lattice Boltzmann-Discrete Element Method (LBM-DEM) could also be used to examine particle-fluid flows. However, the development of such models is still at its infancy. Moreover, it is significantly more computationally demanding than the widely used FVM-DEM method or the Two Fluid Model (TFM) method. It is also not well suited for specific engineering applications such as process modeling and control but it is suitable for fundamental research on particle physics. Moreover, numerical difficulties are inherent in LBM-DEM simulations with strong particle-particle interactions [59, 58]. The literature is devoid of material regarding the development of penalty methods. The development of these methods could then be used to compare against the results of the other multiphase numerical methods such as the CFD-DEM method based on [26]. In particular, there are no studies on mixed resolved-unresolved CFD-DEM method on solid-liquid flows; moreover, there are limited studies on solid-liquid flows using a CFD-DEM, and most of these CFD-DEM investigations on solid-liquid flows are based on fluidized beds. What is more, the literature is devoid of CFD-DEM investigation of solid-liquid flows in complex geometries. Clearly, the development of numerical algorithms to fully resolve multiphase transport in various engineering systems is extremely complex and challenging. [50].

1.2 Objective

Fouling phenomenon is indeed a complex multifaceted problem and it is a subject of debate and ongoing research in various industrial applications such as aerospace. This provides the prime motivation to develop robust and advanced numerical methods to accurately unravel the mechanisms governing multiphase solid-liquid transport and particulate fouling. The development and successful implementation of advanced numerical methods permits engineers, for instance, to better optimize heat exchanger systems for the purposes of fouling alleviation and control. The objective of this investigation is to develop and compare two numerical method to assess the mechanisms that govern two-phase solid-liquid flows and particulate clogging on a filter. The two numerical methods are validated extensively against experimental results.

2 Experimental Method

The experimental investigation of solid-liquid flows is conducted by using the apparatus shown in Figure 2. The experimental rig consists of various components such as the flowmeter, volumetric pump, and the test section, the latter is used to observe the particle accumulation on the filter.

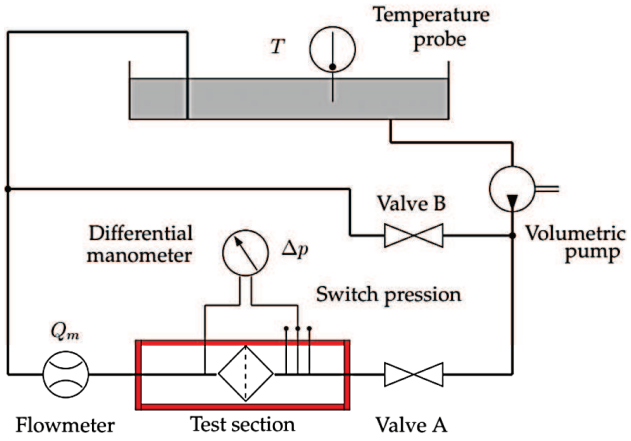

Fig. 2 Diagram of experimental setup

The test section comprises a rectangular tube made of aluminium except for the side walls which are made of plexiglass for visualization purposes. The solid particles are introduced into the test section. The carrier fluid pushes the solid particles away fromt the inlet and towards the filter. Once the particles impact the filter, the particles accumulate and form a granular media. The pressure drop is recorded once the granular structure on the filter remains stationary. The granular profile is then recorded and the pressure drop measured by a differential pressure gauge VEGADIF 65. A RIBILAND PRMCA5AUTO multicellular pump is used to provide a continuous stream of fluid flow at a desired volumetric flow rate. The fluid is sucked fromt he main tank by this multicelluar pump. The fluid flows through the pipes and then returns to the tank. When Valve A is open and Valve B closed, the entire flow passes through the test section. Conversely, when Valve A is closed and Valve B is open, the fluid is directly pushed back into the tank. The flow can be distributed between the two lines by changing the configuration valves. The flow in the test section is measured by a flowmeter electromagnetic OPTIFLUX 2000. It is noted that the accuracy for the OPTIFLUX 2000 and VEGADIF 65 is, respectively, +/- 0.5 % and +/-0.2 %.

Firstly, all the water from the test section is removed. Then, the test section is disconnected from the circuit and its upstream face disassembled. The desired amount of particles is introduced, then the test section is closed and reassembled to the circuit. The tank is finally filled with the desired fluid.

The pump is started, after making sure that both valves are closed. The control valves are positioned to limit the flow in the test section. The fluid is circulated for a few minutes to purge the circuit of the air possibly trapped in the pipes.

The flow rate is regulated by slowly actuating the valves, until the Flowmeter displays the desired value. Once the system is stabilized, the loss of load (i.e. pressure drop) is recorded on the differential pressure gauge, and the profile of the particle cluster is photographed. This step is repeated for several flow values.

A summary of the experimental protocols for each test case, based on a specific volumetric flow rate, and particle volume, is:

- Purge the whole system
- Insert the desired amount of particles
- Fill the loop with tap water
- Close vane A and open vane B
- Start the pump
- Open slightly vane air to allow flow in the test section
- Wait until all the air exit the system
- Adjust vane A to set the desired volume flow rate
- Wait until the particles and the pressure drop stabilize
- Record the pressure drop and take a picture of the particles

3 Numerical methods

The methods presented in this section are developed and implemented in a research C++ based CFD program with an overarching goal of simulating these transient, complex flows in jet engine fuel system geometries [31]. We investigate solid-liquid flows and solid particle accumulation on a filter based on two numerical methods. Section 2.1 covers the equations based on the mixed resolved-unresolved CFD-DEM method. Section 3.2 covers the unresolved coupled CFD-DEM method developed in Open Field Operation and Manipulation (OpenFOAM), an opensource C++ CFD program. The presence of non-reactive dense particulate-fluid flows in a jet-fuel filter system signifies the necessity to accurately resolve interactions between the individual particles and the hydrodynamic interactions between the particles and carrier fluid (two-way coupling) and particle and the walls of the domain (four-way coupling) which is the main focus of this work.

3.1 Mixed resolved-unresolved CFD-DEM method

The transport of incompressible and isothermal fluid is governed by the Navier-Stokes equations, and is given as

$$\nabla \cdot (\mathbf{v}) = 0 \tag{1}$$

$$\frac{\partial(\rho_f \mathbf{v})}{\partial t} + \nabla \cdot (\rho_f \mathbf{v}\mathbf{v}) = -\nabla(p) + \nabla \cdot (\mu \nabla^2(\mathbf{v})) + (\rho_f \mathbf{g}) + F_{pf(B)} \tag{2}$$

where $\mathbf{v}$ is the fluid velocity, fluid density ρ_f, fluid pressure p, gravitational acceleration g, fluid dynamic viscosity μ.

The clogged filter comprises a stack of ice crystals of various sizes (c.f. Figure 1). The feedback of the particles on the fluid flow must be considered at two scales:

- Microscopic: ice particles are intrinsically porous. Experiments have shown that the fraction of fluid within the ice can reach up to 50
- Macroscopic: Even if the particles were impermeable, the stack of particles has interstices in which the fluid can flow.

The pressure drop related to the intrinsic porosity is modelled by Darcy's law. For a given finite volume cell of the mesh, the pressure gradient related to viscous loss is expressed:

$$\nabla p = -\frac{\mu}{K}(v_f - v_s), \tag{3}$$

where μ is the dynamic viscosity of the fluid, v_f the superficial velocity of the fluid, v_s is the (average) solid velocity within the cell, and and K is the intrinsic permeability. To account for the macroscopic effects, equation (3) is weighted by a *permeability function* $\wp$, calculated for each mesh cell :

$$\nabla p = -(\wp)(\chi_s)\frac{\mu}{K}(v_f - v_s), \tag{4}$$

where χ_s is the solid volume fraction, defined as the ratio of the total volume of particles entirely or partially located in a computational cell (c.f. Figure 3), to the volume of the CFD cell:

$$\chi_s = 1 - \alpha_d = \sum_{i=1}^{k_c} \frac{V_i}{\Delta V_c}. \tag{5}$$

The permeability function used in the present work is a power law of exponent $\eta = 2$, which acts as a tuning parameter for the macroscopic porosity. The final expression for the momentum sink term is:

$$F_{pf(B)} = -\chi_s^{\eta}\frac{\mu}{K}(v_f - v_s) \tag{6}$$

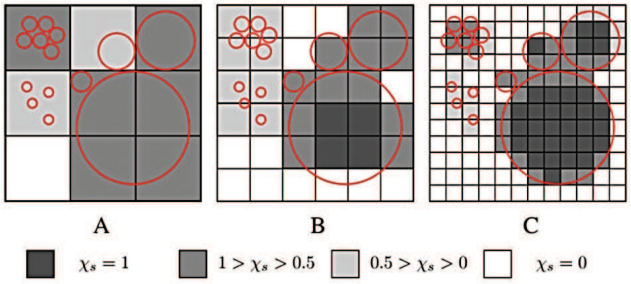

Fig. 3 Each cell is coloured according to its solid volume fraction χ_s. The difference between the particle size and the resolution of the mesh has an impact on the choice of the coupling method. A) Most particles are smaller than the mesh cell size, therefore an unresolved approach is suitable. B) The particles and the mesh cells have similar size. Neither approach is appropriate but the hybrid method is applicable. C) The flow around the largest particle can be resolved accurately.

It is noteworthy that the mixed resolved-unresolved CFD-DEM method presented in Section 3.1 is mathematically equivalent to the brinkman penalization technique implemented by Piquet et al. (2016) [41]. The Brinkman penalization cannot solve for particles being larger than the mesh cell size. However, the method described herein is capable of fully resolving the fluid flow around the particle irrespective of the grid resolution.

3.1.1 Hydrodynamic forces

The forces considered in this work include the effects of pressure field, buoyancy and drag. For the sake of simplicity, the other hydrodynamic forces and the effects related to the particles rotation are not taken into account. Since the particles accumulate, their interactions with each other and with the walls must also be considered. The contact force between a particle **i** and an other solid **k** in the simulation is denoted F_{ik}^c. The constitutive laws that govern the transport of the individual discrete particles are based on Newton's second law given as:

$$m_i \frac{dv_i}{dt} = F_g + F_d + F_p + \sum_{k \neq i} F_{ik}^c \tag{7}$$

The buoyancy force F_g is expressed as a function of particle mass m_p, fluid density ρ_f, particle volume V_p, and gravity g and is given as:

$$F_g = (m_p - \rho_f V_p)g. \tag{8}$$

The drag force is given as

$$F_d = -\frac{1}{2}\rho_f S_p C_D \|V_r\| V_r, \tag{9}$$

where C_D is the drag coefficient, S_p is the particle cross sectional area, and V_r is the relative speed of the particle which is equivalent to $V_p - V_f$. The effect of the pressure field is denoted by

$$F_p = -V_p(\nabla p)_{hydro}, \tag{10}$$

where ∇p is the pressure gradient. In this study, the particles are assumed smooth, rigid, and isothermal.

3.1.2 Particle interactions

There are two main approaches for modelling contact particle interactions. The first relies on the conservation of the momentum of binary and instantaneous shocks, and generally implements algorithms based on the management of collision events. It is well suited for inelastic collision of hard spheres. In event-driven algorithms, the time step is determined by the smallest duration between two contacts, which tends to zero when the solid fraction increases. In the second approach, two particles are considered in contact when they interpenetrates slightly. Normal and tangential forces are then evaluated by a spring-dashpot model.The cohesive contacts (i.e. cohesion energy density) between the particles and walls have not been taken into account because the particle diameter is significantly greater than 1 μm. In this study, the density and diameter of the glass particles is set to 2500 kg/m^3 and 2 mm respectively.

Industrial applications of clogging require simulations over periods of several seconds and involves locally high concentrations of particles. The very small time-step of conventional models can become problematic. A contact algorithm for inelastic collisions allowing for larger time steps was thus developed. The present method consider that the collisions between particles are perfectly inelastic. This choice is based on two arguments : 1) The coefficient of restitution for wet particles and particles in fluid is much lower than dry particles [29] 2) The experimental setup is designed to study static stacks of particles.

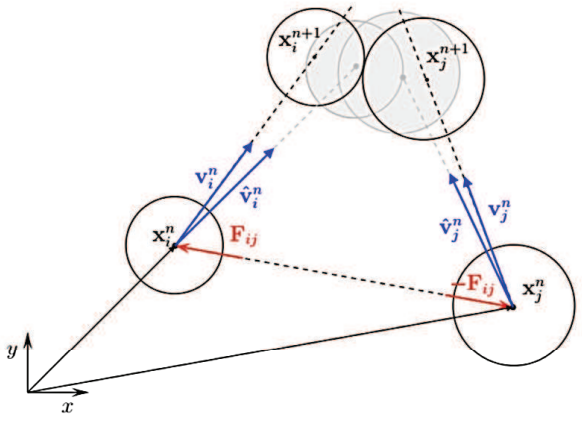

Fig. 4 Clogging of a typical fuel filter [31].

The principle of the model is as follows: First, we consider a pair of particles (i, r_i, m_i) and (j, r_j, m_j) where r and m refers to radius and mass. In the absence of any interaction force, interpenetration between two particles at the end of a time step dt may occur, as shown in Figure 4. The principle of the contact handling algorithm is to compute the contact force F_{ij}^c required to prevent this behaviour for each pair of particles and to apply it before the position of the particles are updated. In principle, the mixed resolved-unresolved CFD-DEM method models the circular particles using an immersed boundary (IB) type method, and the discrete element method (DEM) is used to enforce a 'moving' immersed boundary to deal with particle motion and particle interactions. The particles provide the valuie of the χ_s^η function (c.f. Equation 6) within the domain.

The derivation of the method starts with the discrete equation of motion for a pair of particles:

$$\begin{cases} \dfrac{X_i^{n+1} - X_i^n}{dt} = V_i^n + \frac{\Delta t}{m_i}(F_i^h + \sum\limits_{k \neq i} F_{ik}^c) \\ \dfrac{X_j^{n+1} - X_j^n}{dt} = V_j^n + \frac{\Delta t}{m_j}(F_j^h + \sum\limits_{k \neq j} F_{jk}^c) \end{cases} \tag{11}$$

Where F_i^h refers to the sum of all but contact forces. Here a 1st-order forward euler formulation is used but the method can be derived with more refined time schemes. The distance that would cover a particle if there was no contact divided by the time step dt is called predicted velocity and denoted $\hat{v}$. The expression reads:

$$\hat{v}_i^n = v_i^n + \frac{\Delta t}{m_i} F_i^h \tag{12}$$

Thereafter, let us denote any relative quantity $\phi_{ij} = \phi_j - \phi_i$. The two vector equation of motion are subtracted from one another and projected on the normal direction n_{ij} to obtain a single scalar equation :

$$x_{ij}^{n+1} \cdot n_{ij} = x_{ij}^{n} \cdot n_{ij} + \Delta t \hat{v}_{ij} \cdot n_{ij} + \left(\sum_{k \neq i} \frac{\Delta t^2}{m_i} F_{ik}^c + \sum_{k \neq j} \frac{\Delta t^2}{m_j} F_{jk}^c \right) \cdot n_{ij} \quad (13)$$

$x_{ij} = (X_j - X_i) \cdot n_i j$ is the relative distance between two particle and $\hat{v}_i j = (\hat{v}_j \hat{v}_i) \cdot n_i j$ the relative predicted velocity projected along n_{ij}. Decomposing contact forces by their amplitude f_{ik} and direction n_{ik} and introducing previous notations, equation (12) becomes:

$$x_{ij}^{n+1} = x_{ij}^{n} + \hat{v}_{ij} \Delta t + \left(\sum_{k \neq i} \frac{\Delta t^2}{m_i} f_{ik} n_{ik} + \sum_{k \neq j} \frac{\Delta t^2}{m_j} f_{jk} n_{jk} \right) \cdot n_{ij} \quad (14)$$

Avoiding the interpenetration at the end of the next time step is equivalent to verifying for each pair of particle (i, j) the inequality:

$$x_{ij}^{n+1} \geq r_i + r_j \quad (15)$$

Combining eq (14) and eq (15) finally gives:

$$x_{ij}^{n} + \hat{v}_i j \Delta t + \left(\sum_{k \neq i} f_{ik} \frac{\Delta t^2}{m_i} n_{ik} \cdot n_{ij} + \sum_{k \neq j} f_{jk} \frac{\Delta t^2}{m_j} n_{jk} \cdot n_{ij} \right) \geq r_i + r_j \quad (16)$$

The distance between the surface of two particles is usually denoted δ_{ij}. For the sake of conciseness, we denote:

$$\Lambda_{ik}^{j} = \frac{\Delta t^2}{m_i} n_{ik} \cdot n_{ij} \quad (17)$$

Equation 15 holds for each pair of particles. A system of inequalities $g(f_{ij})$ is obtained:

$$g(f_{ij}) = \delta_{ij} - \hat{v}_{ij} \Delta t - \left(\sum_{k \neq i} \Lambda_{ik}^{j} f_{ik}^{k} + \sum_{k \neq j} \Lambda_{jk}^{i} f_{jk}^{k} \right) \leq 0 \quad (18)$$

Adding contact forces will impact the total kinetic energy of the particle system. Therefore, the contact forces must be computed so that the set of constraint is satisfied while minimizing the change of kinetic energy. This is achieved through an iterative procedure, fully described in [31]. Starting from zero, contact forces are gradually increased in proportion of the value of the constraint functions. After convergence, the speed of a particle a time $t + \Delta t$ is computed with the resulting interactions forces:

$$v_i^{n+1} = \hat{v}_i^{n} - \frac{\Delta t}{m_i} \left(\sum_{k \neq i} f_{ik} n_{ik} \right) \quad (19)$$

In practice, the convergence of the method requires an under-relaxation of parameter ω. The iterative procedure is as follow:

1. Initialisation of forces and constraints:

$$f_{ij}^{0} = 0; \qquad g_{ij}^{0} = \delta_{ij} - \hat{v}_{ij} \Delta t \quad (20)$$

2. Update forces :

$$f_{ij}^{k+1} = max(0; f_{ij}^{k} - \omega . g_{ij}^{k}) \quad (21)$$

3. Update constraints:

$$g_{ij}^{k+1} = \delta_{ij} - \hat{v}_{ij} \Delta t - \left(\sum_{k \neq i} \Lambda_{ik}^{j} f_{ik}^{k+1} + \sum_{k \neq j} \Lambda_{jk}^{i} f_{jk}^{k+1} \right) \quad (22)$$

4. Convergence test

3.1.3 Numerical schemes and resolution algorithm

The complexity of solving the Navier-Stokes equations lies in the absence of an independent pressure equation, whose gradient plays a dominant role in the three momentum equations. Moreover, the continuity equation no longer behaves like a transport equation for the mass, but plays the role of constraint on the velocity field. Thereby the main difficulty in solving the incompressible Navier-Stokes equations is the calculation of the pressure field. The resolution algorithm adopted in this work is based on the SIMPLE algorithm, first developed by [6], and adapted to unstructured meshes by Rhie and Chow [46]. The reader is referred to Ferziger and Peric [15] regarding the standalone SIMPLE or PISO algorithms.

Due to the non-linearity of the equations, this class of algorithms involve an iterative procedure to achieve coupling between pressure and velocity fields. The deferred correction is a technique whose principle is to calculate higher order terms explicitly, and treat them as a source term in the second member of the equation. A low-order approximation of these terms is treated

implicitly in the first member, and subtracted from the second member. As the iterative procedure converge, low-order terms tend to zero. In this work, we used a moving least square (MLS) interpolation scheme developped by Cueto-Felgueroso et al. for compressible flow [7] and applied to incompressible flow by Ramírez et al. [44]. A deferred correction is used for the calculation of convective flux. The low implicit term is a Linear Upwind Scheme, and the explicit correction is a second order MLS interpolation. The diffusive flux is directly calculated by a second order MLS interpolation. The volume integrals for the temporal term and the source term are approximated by a midpoint rule. A second order backward Euler scheme is used for time derivatives.

The linear algebra is handled through the Petsc library [4]. The three linear systems resulting from the (uncoupled) momentum equations are solved by the Bi-Conjugate Gradient Stabilized (BiCGSTAB) method with block-Jacobi preconditioning. The pressure-correction equation is solved by Hypre's algebraic multi-grid (AMG) method.

3.2 Unresolved CFD-DEM method

3.2.1 Development of an unresolved CFD-DEM

The numerical results obtained using the method in Section 2.1 is compared against the numerical results based on a coupled CFD-DEM method developed on the OpenFOAM platform, an open-source C++ based CFD program. In this study, the particles are smaller than the CFD mesh cell size, therefore the coupling between the CFD and DEM is achieved with an unresolved method, developed on the OpenFOAM platform [38].

The transport of incompressible and isothermal fluid is governed by the Navier-Stokes equations, and is given as

$$\frac{\partial \alpha_d}{\partial t} + \nabla \cdot (\alpha_d v) = 0 \tag{23}$$

$$\frac{\partial (\rho_f \alpha_d \mathbf{v})}{\partial t} + \nabla \cdot (\rho_f \alpha_d v v) = -\nabla(\alpha_d p) + \nabla \cdot (\alpha_d \tau) + (\rho_f \alpha_d g) + F_{pf} \tag{24}$$

where α_d is the fluid volume fraction, fluid velocity $\mathbf{v}$, fluid density ρ_f, fluid pressure p, gravitational acceleration g, fluid viscous stress tensor τ. The gas volume fraction is given as

$$\alpha_d = 1 - \sum_{i=1}^{k_c} \frac{V_i}{V_c} \tag{25}$$

where V_i is the volume of a particle i, ΔV_c is the volume of the computational cell, and k_c is the total number of particles in a computational cell. The interphase momentum transfer between the particles and fluid is denoted by F_{pf} [26] and is given as

$$F_{pf} = \frac{1}{\Delta V_c} \sum_{i=1}^{k_c} f_{pf,i} \tag{26}$$

In this study, the sink term F_{pf} accounts for gravity force, drag force, lift, and pressure gradient force, virtual mass, and Basset history forces. Brownian force is neglected as the size of particles in both numerical methods is significantly greater than 1 μm. It is noteworthy that the fluid phase is modelled by equations 23 and 24, and assinging $\alpha_d = 1$ in the entire domain becomes equivalent to the mixed resolved-unresolved approach described in Section 2.1. The particularity of this method comes from the asymmetry in the treatment of the interphase momentum transfer : The action of the flow on the particles F_{fp} is modelled as in typical unresolved approach, while the sink term in the momentum equation F_{pf} is calculated based on the local medium porosity, in the manner of resolved methods. For a complete description of the method, see [30] and [31].

A soft-sphere DEM method, similar to the Cundall and Strack model [8], in the form of spring-slider-dashpot model is employed to accurately resolve the trajectories of particle motion by integrating the Newtonian equations of motion. The soft-sphere approach permits one to explicitly define the properties of both particle and wall (i.e. density, Young's modulus, Poisson ratio), and also the coefficient of restitution, coefficient of friction, and cohesion energy density between particle-particle and particle-wall interactions.The following equations are used to model the particle-particle and particle-wall interactions [26].

The equations governing the motion of solid particles is given as:

$$m_i \frac{d\mathbf{V_{ip}}}{dt} = m_i \mathbf{g} + \sum_{j=1}^{k_i} \mathbf{F_{C,ij}} + \mathbf{f_{pf,i}}, \tag{27}$$

$$I_i \frac{d\omega_i}{dt} = \sum_{j=1}^{k_i} \mathbf{T_i}, \tag{28}$$

where V_{ip} is the translational velocity of a particle, and the number of particles in contact with particle i is denoted as k_i, I_i is the moment of intertia, rotational velocity ω_i, and torque T_t.

The normal contact force is given by

$$F_{cn,ij} = (-k_n \delta_{nij}^{1.5} - \eta_n u_{ij} \cdot n_{ij}) n_{ij}, \tag{29}$$

The tangential force is given by

$$F_{ct,ij} = (-k_t \delta_{tij} - \eta_t u_{sij}), \tag{30}$$

where k_n is the non-linear normal spring stiffness, and k_t is the tangential spring stiffness between particle contacts i and j. The following expressions connote the spring stiffness:

$$k_n = \frac{4}{3}\sqrt{R^*}\frac{E}{2(1-\sigma_j^2)}, \tag{31}$$

and

$$k_t = 8\sqrt{R^* \delta_{nij}}\frac{G}{2(2-\sigma)}, \tag{32}$$

where

$$R^* = \frac{r_i r_j}{r_i + r_j} \quad and \quad G = \frac{E}{(2(1+\sigma))}, \tag{33}$$

where δ is the deplacement, unit vector n_{ij} from the centres of particles i and j. The slip velocity of the contact point is given as:

$$u_{sij} = u_{ij} - (u_{ij} \cdot n_{ij}) n_{ij} + (r_i \omega_i + r_j \omega_j) \times n_{ij}, \tag{34}$$

where u_{ij} is the relative velocity vector between the contact of particles i and j.

For particle sliding to occur, the following relation must be satistifed:

$$|F_{ctij}| > \mu_f |F_{cnij}| \tag{35}$$

The resultant tangential force is expressed as a function of the friction coefficient μ_f:

$$|F_{ctij}| = -\mu_f |F_{cnij}| u_{sij} / |u_{sij}|, \tag{36}$$

The damping coefficient is given as

$$\eta_n = \lambda (m^* k_n)^{0.5} \delta_n^{0.25}, \tag{37}$$

where m^* is the effective mass and expressed as

$$m^* = \frac{m_i m_j}{m_i + m_j}, \tag{38}$$

where m_i and m_j is, respectively, particles i and j. It is noteworthy that the emperical constant λ is related to the coefficient of restitution. Moreover, the damping coefficient η_n is assumed to be identical to η_t.

In order to accurately capture particle contacts, the DEM time-step must be around 10 - 100 times smaller than the CFD time-step [57]; as such, the CFD time-step is set at 1 x 10^{-5} s whereas the particle (discrete phase) collision resolution time-step is set to 20. The simulation is run from 0.00 s to 5.00 s and the particle injection commences at 0.20 s to allow for fluid flow development prior to the injection of particles. The particle velocity is initialized at the same velocity as the fluid velocity. The Young's Modulus is assigned a slightly lower value than the actual to reduce computational effort. Trial numerical results show negligible difference in the particle distribution patterns irrespective of the Young's Modulus value. The same observation is reached by Tsuiji et al. [51, 52].

The presence of non-reactive dense particulate-fluid flows signifies the necessity to accurately resolve interactions between the individual particles and the hydrodynamic interactions between the particles and carrier fluid (two-way coupling) and particle and the walls of the domain (four-way coupling). The cohesive contacts (i.e. cohesion energy density) between the particles and walls have not been taken into account because the particle diameter is significantly greater than 1 μm. In this study, the density and diameter of the glass particles is set to 2500 kg/m^3 and 2 mm respectively.

The coupling between the two phases is achieved as follows: first, at each time-step, the DEM solver will relay the dynamic information such as positions and velocities of individual particles, in order to evaluate the porosity and the particle-fluid interaction force in a computational cell. Afterwards, the CFD solver will use this data to evaluate the gas flow field which computes the fluid forces acting on each DEM particle. Then all of these resultant forces are imported into the DEM in order to generate motion information of individual particles for the next time-step. The fluid force acting on each discrete particle will act in response on the carrier fluid from the DEM particles, thereby complying with Newton's third law of motion [42].

3.2.2 Mesh cell size and DEM particle size

Although it is desirable to have a fine mesh in order to resolve the full details of the fluid flow field, the numerical stability becomes a concern if the size of a discrete particle is identical or greater than the size of a computational cell. To circumvent this issue, smoothing or approximation models are deployed into the numerical model. The reader is referred to Goniva et al [22] regarding other approximation methods (such as big particle void fraction method, divided void fraction method, etc) for use in the event a DEM particle is either very similar to the cell size or slightly exceeds the cell size. In this study an approximation method based on Wahyudi et al [53] is developed in OpenFOAM. This approximation method is based on the designation of the maximum solid phase fraction per computational cell if the CFD cell is completely smeared with the DEM particle; additionally, the mass and momentum sources are distributed to neighbouring cells as a means to conserve mass and energy [53].

It is noteworthy that there is no concrete consensus among the research community regarding the preferred ratio of the mesh cell size to the particle diameter; values vary in literature. For instance, Li et al [28] suggested a ratio of 1.670 or above whereas both Geng & Che [16] and Wang et al [55] successfully used 1.00 and 1.33 respectively, whereas Feng & Yu [14] used 1.625. Kubicki & Lo [24] numerically examined slurry transport with an S_c/D_p ratio of approximately one and it was found the numerical results are in good agreement with the experimental data. Kuruneru et al. [25] showed no difference in the particulate foulant distribution profiles in an idealized metal foam heat exchanger pertaining to a mesh cell size/particle diameter ratio of 1:1 or higher. What is more, Li et al [28] claimed that a ratio of 1.67 or higher is suitable (at least for their study) as the results corresponding to about 50 data points are all identical to the experimental results; interestingly though, about 68 % and 74 % of the data points corresponding to ratios of 1.02 and 1.12 respectively, closely match the experimental data points. All 48 data points for ratios of 1.67 or higher identically match the experimental data. Wahyudi et al [53] used very fine grids near the wall of a fluidized bed in order to thermally resolve the boundary layer. It is in this region that the particle diameter is smaller than the mesh cell size (half the particle diameter). However, in the study by Li et al [28], the minimum gas phase fraction was not specified; moreover, the 1.67 ratio is based on the Gidaspow drag law (ErgunWenYu) [17], as such it remains to be seen whether the same ratio stands for other drag closures (i.e. Di Felice [10], PlessisMasliyah [11], Koch & Hill [23]) or a standard drag model. What is more, the Gidaspow model is not universally used in all dense particle-fluid systems. To be precise, the Gidaspow is ideally suited for packed beds whereas the Di Felice drag closure is derived for particle sedimentation. Thus, the 1:67 ratio ideally should not be used in all dilute or dense granular-fluid systems. The interested reader is referred to [27] regarding grid size to DEM particle diameter ratio and validation of numerical model pertaining to particel bounce in a rectangular model compared with experimental data. In fact, there is no concrete consensus among the research arena regarding the modeling of solid-air drag closures [12, 48, 18].

3.2.3 Numerical solution and algorithm control

A generalized (GAMG) solver and a Gauss-Seidel smoother is deployed to solve the pressure equation. For the solution of the momentum equation, a smooth solver with a smoother symmetric Gauss-Seidel (sGS) is used while performing a single sweep smoothing iteration prior to re-calculating the residual in order to improve computational efficiency. These solvers operate on a LDU matrix class where the smooth solver is for symmetric and asymmetric matrices, and the smoother converges the solution to the required tolerance (or relative tolerance). The GAMG solver generates a solution on a mesh with a small number of cells with minimal computational effort; afterwards, the solver maps the solution onto a finer mesh which uses it as a starting solution in order to generate an accurate solution on the fine mesh. This is achieved by geometrically coarsening the grid (geometric multi-grid) or directly harnessing the algebraic multi-grid irrespective of geometry. The mesh is coarsened or refined in steps. The agglomeration of cells is executed by a 'face area pair' agglomerator. Merge levels is set to control the pace at which coarsening or refinement of the grids is performed. Typically in most situations, OpenFOAM coarsens/refines the grid one level at a time by making one cell out of four (i.e. mergeLevel 1). This level or merging generally yields optimal convergence. However, for cases with a simple mesh, coarsening (or refining) of the grids can be safely achieved at a rapid pace by coarsening (or refining) two levels at a time (i.e. mergeLevel 2) [39, 38].

3.2.4 A merged SIMPLE-PISO (PIMPLE) algorithm

The modular implementation and versatility of OpenFOAM permits one to implement a hybrid SIMPLE-PISO (PIMPLE) algorithm [39, 38]. This algorithm is used to couple the pressure-velocity equations for transient solutions with very large Courant numbers (1-10) which in turn assists in stabilizing the numerical

convergence while preserving numerical accuracy. The PIMPLE algorithm consists of various important parameters that could be used depending on the case study. These parameters include the number of non-orthogonal correctors, number of correctors (inner loops-pressure correction), number of outer correctors (outer loops-pressure-momentum correction), momentum predictor, consistent (PIMPLEC), residual controls, under-relaxation. PIMPLEC (PISOC-SIMPLEC) is beneficial for cases with a large maximum Courant number (Co). Although the PIMPLEC algorithm is applicable for transient solutions with very large Courant number, simulations with this algorithm take longer to reach convergence compared with the SIMPLEC algorithm. This is due to the fact that the PIMPLEC algorithm involves both predictor and corrector steps. Unlike the standalone PISO algorithm, which is generally applicable for cases where $Co \leq 1$, the PIMPLE algorithm permits the use of a high time-step or an adaptive time-step (i.e. assign a maximum Courant number) to numerically stabilize transient solutions which is beneficial for cases involving complex fluid flow patterns in complex geometries with skewed non-orthogonal meshes. It is also beneficial for particle-laden gas flows based on unstructured meshes where the DEM particle size is on par with the CFD mesh cell size. Executing the pimple algorithm loops over the PISO algorithm in one time-step which permits some under-relaxation between these loops. This activity permits the use of larger time-steps, which is not possible in the standalone PISO algorithm. The PIMPLE algorithm attempts to solve the momentum equation one or more time at each time-step depending on the number of outer correctors assigned to the PIMPLE loop. In other words, the number of outer correctors defines the quantity of outer iterations until time step convergence is realized, namely, the number of times the system of equations are performed prior to advancing to the subsequent time step irrespective of whether that time step has converged or not. In this scenario, the time step convergence is based on the absolute tolerance (i.e. 1 x 10^{-5}). In theory, the PIMPLE algorithm is identical to the PISO algorithm if one outer corrector is assigned. This is in theory identical to multiple PISO loops per time-step analogous to a transient SIMPLE algorithm. In other words, assigning only one outer correctors solves the momentum equation once only at each time-step which is the norm in a PISO algorithm. In the event the pressure-momentum coupling is calculated only once (one outer corrector), the standalone PISO algorithm is enforced irrespective of the number of correctors (1-3). The number of times the pressure is corrected within an iteration depends on the number of inner correctors and is ususally assigned a value between 1-3.

The number of correctors signifies the number of times the pressure field is corrected. For tetrahedral non-orthogonal mesh, a correction term is essential for the treatment of non-orthogonality. In other words, the number of non-orthogonal correctors corrects the solution Laplacian term of the pressure equation (surface normal gradient schemes). The value is ranges from 0 to 2; it is generally set to 0 for steady-state simulations and pure hexahedral mesh or 1 for transient and/or low-quality highly skewed meshes (i.e. max non-orthogonality angle is approximately 70° or higher). In this study, 2 correctors and 2 non-orthogonal corrector is assigned. For SIMPLE to be switched to PISO mode, it is necessary to include at least an additional pressure and velocity corrector. The PISO algorithm is a non-iterative procedure; as such, the inclusion of more than 1 outer-correctors infers a iterative PISO algorithm or PIMPLE algorithm. The pressure is re-calculated based on the updated fluxes obtained from the outer loop correction. For example, in this study, OpenFOAM computes 50 SIMPLE outer loops and within one outer loop, the pressure is corrected twice. The number of outer correctors must be set to 50 or greater which is the recommended quantity [39, 38]. To ensure the robustness and stability of the PIMPLE algorithm, under-relaxation factors for outer iterations is enforced.

An under-relaxation factor is assigned to under relax the system of discretized equations. An under-relaxation factor is assigned to under relax the system of discretized equations (eq. 3.95 & 3.96 pp.115 [20]); moreover, an under-relaxation factor is also used to relax the new pressure equations. In other words, solving the pressure equation again is executed in order to yield a better approximation of the correct pressure fields (eq. 3.145 pp.149 [20]). If the number of outer correctors is set to 50, the PIMPLE algorithm will solve for the first 49 with relaxation factors only. The under-relaxation factor for the final equations and fields of velocity and pressure is set to 1 in order to comply with the conservation of mass. It is noteworthy that the PISO algorithm does not under-relax the fields and equations and the momentum corrector step is executed more than once. Likewise, the pressure-momentum correction (outer loops) is essentially a SIMPLE loop which requires under-relaxation to stabilize the solution. The number of outer correctors (outer loop correction) is set as the number of times the fluxes, pressure, and momentum are re-calculated within one time-step. However, slightly lower final residuals could be enforced only if a very high number of outer correctors ($\geq$ 100) is assigned to find the correct solution within one time-step.

Secondly, a residual sub-control is enforced for the PIMPLE algorithm in order to reduce the computational time whilst maintaining numerical stability. This allows OpenFOAM to exit the PIMPLE outer corrector loop once a solution fulfils the residual criteria during a time-step. A residual and tolerance criteria for both the PISO and PIMPLE loop/iteration is assigned, where OpenFOAM will escape the PISO loop/iteration when the final residuals within each PISO loop fall below the assigned final tolerance level. For instance, the geometric agglomerated algebraic multi-grid (GAMG) solver will iteratively solve the system of linear equations until the final residual for pressure falls below an allocated value (i.e. 1 x 10^{-6}) OpenFOAM will escape the PIMPLE loop and proceed to the next time-step if the initial residuals fall below the allocated tolerance value. The deployed PIMPLE algorithm is well suited for skewed complex geometries and meshes and multiphase transport (with a slightly high Courant number). As the case study involves transient simulations, the relative tolerance is set to 0.0 to yield efficient PIMPLE simulations by forcing the solution to converge to the solver tolerance in each time step [37]. The residuals for the pressure and velocity is set to 1 x 10^{-6} and 1 x 10^{-5} respectively whereas the residual control for the PIMPLE loop is assigned as 1 x 10^{-3} for both pressure and velocity.

3.2.5 Numerical schemes

There exists an array of numerical schemes in OpenFOAM [39]. For most practical engineering applications, the following schemes shown in Table 1 are used. Linear interpolation is widely used in a number of cases although a cubic interpolation could be deployed but it is rarely used except for very cases such as stress analysis. The corrected surface normal gradient schemes is generally used for most cases where the maximum mesh non-orthogonality does not exceed 70˚which is the case in our study.The uncorrected and orthogonal surface normal gradient schemes is normally deployed in the even the mesh exhibits very low non-orthogonality (i.e. ≤ 5˚). The choice of the Laplacian scheme is also based on the maximum mesh non-orthogonality. A Gauss Linear corrected Laplacian scheme is deployed to obtain solution to the pressure poisson equation. A second order accurate is employed for the divergence schemes. A bounded first order implicit Euler scheme are deployed for the time derivatives. Other temporal discretization schemes include the second order unbounded implicit scheme which is similar to the linear multistep Adams-Moulton scheme, and the second order bounded implicit Crank-Nicolson scheme. The Crank-Nicolson scheme comprises a blending factor from 0 to 1. A pure Euler scheme is equivalent to the Crank-Nicolson scheme with blending factor of 0, whereas a pure Crank-Nicolson scheme is based on a blending factor of 1. For the numerical schemes for the particles, an Euler-implicit integration scheme is used. The coupling between the two phases permits the transfer of the corrected momentum from the discrete phase to the fluid continuum phase.

Terms	Numerical Schemes
1^{st} & 2^{nd} order time derivatives	Euler
Gradient schemes	Gauss linear
Divergence schemes	Gauss linear upwind unlimited
Laplacian schemes	Gauss linear corrected
Interpolation schemes	Linear
Surface normal gradient schemes	Corrected

Table 1 OpenFOAM Numerical Schemes

A recent study has found that the commercial software FLUENT-EDEM exhibits a miscalculation of the drag force (to a certain degree) which resulted in the overestimation of the mean particle velocity, which is attributable to the lack of an appropriate mesh interpolation scheme in their code [12]. In short, the velocity of gas is not interpolated to the particle location, and all of the solid particulates in the CFD grid encounter identical fluid velocity irrespective of the particle position within the fluid mesh cell [12]. OpenFOAM circumvents this issue by explicitly enforcing an interpolation scheme based on the carrier fluid bulk properties (i.e. fluid density, velocity, and dynamic viscosity). The reader is referred to Elghobashi (1994) [13] and Xiao & Sun (2011) [56] for additional details on these interpolation schemes. As the simulation is fully coupled, the momentum correction is transferred from the discrete solid phase to the fluid continuum phase. The discrete phase is coupled to the carrier phase (i.e. source terms are generated for the carrier phase via a semi-Implict scheme).

3.2.6 Computational domain and boundary conditions

A schematic of the geometry used for both numerical methods is shown in Figure 5. The filter is composed of wires (300-500 μm diameter) and it forms square holes (500-800 μm). The filter permeability is set to 1 x 10^{-10} m^2. The geometric morphology is identical to the geometry of the test section used for the experimental investigation given in Figure 2.

The inlet velocity is set to 0.885 m/s which corresponds to a volumetric flow rate of 4 m^3/h. No-slip

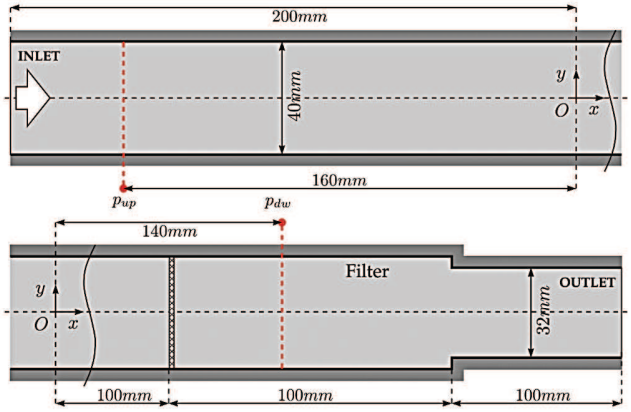

Fig. 5 Computational domain

walls are enforced on the top and bottom of the channel.

4 Results & Discussions

We compare the numerical and experimental particle distributions in three different cases as shown in Figure 6 & Figure 7. Four different solids volume are investigated: 2 mL, 4 mL, 6 mL, 8 mL. The numerical pressure drop is evaluated and compared against the experimental values, as shown in Figure 7. The profile of the cluster formed by particles on the filter results from the balance between hydrodynamic forces, the effect of gravity, the interaction between the particles, and the volume of each type of ball, as shown in E1 and E2 in Figure 6. As time elapses, the solid particles aggregate and eventually clog the filter. Particle aggregate spread along the horizontal (x-axis) and vertical direction (y-axis), based on two solids volume 4 mL and 8 mL, is in good agreement with the experimental results, as shown in Table 2. According to Figure 7, the pressure drop aligns well with the experimental observations based on a solid volume of 2 mL or 4 mL. However, there exists a large discrepancy between the experimental and numerical pressure drop at 6 mL and 8 mL. Additional simulations have shown that the solution greatly underestimates the pressure drop at a large solid volume (i.e. 8 mL , 10 mL) irrespective of the inlet velocity. However, this is not the case for lower solid volume (i.e. 2 mL and 4 mL). The pressure drop miscalulation stems from the fact that total number of particles injected into the 2D configuration is not the same as a 3D configuration (experiments - Secion 3.1, 3.1.1). Instead, a homogeneous repartition of the particle along depth of the experimental test channel is assumed and the equivalent surface of the particles in a 2D case is computed as ($S_s = V_s/L$) as specified in Section 2.

In 2D calculation, an artificial porosity is added to the particle in order to account the 3D effect. Although this assumption showed large discrepancy between the numerical and experimental pressure drop values in OpenFOAM, the mixed resolved-unresolved CFD-DEM technique yield reasonably accurate numerical pressure drop results. However, it is noteworthy that although the mixed resolved-unresolved CFD-DEM technique yields very accurate representation of the particle spread distribution profile, the mixed resolved-unresolved CFD-DEM technique did show large discrepancy between the numerical and pressure drop distributions in several cases. This discrepancy stems from the fact that an ideal filter is used which actually blocks the particles but does not impede the incoming carrier fluid. Secondly, the introduction of significantly fewer particles into the 2D system results in a loosely packed particle aggregate bed formation (i.e. aggregate structure is less compact) which consists of more voids between the particle contacts (O1) than the 3D case (E1); moreover, tightly packed particles or compactness of the 3D case (i.e. E1) infer the particles being motionless, whereas the 2D case (i.e. O1) it was observed that the particles undergo very faint unsteady sliding vibration-like movement. Notwithstanding the subtle discrepancies in the numerical results, the overall solid-liquid distribution such as the particle distribution spread, and the pressure drop is in reasonably good agreement with the experimental results.

As shown in Figure 7, at 6 mL and 8 mL solids volume, a slightly better agreement is observed between the experimental and the mixed resolved-unresolved CFD-DEM method. However, the large discrepancy in the OpenFOAM results is linked to the 2D particle projection assumption in addition to the difference in velocities of the particles together with the compactness of the 2D and 3D cases. At 8 mL solids volume, both numerical methods greatly miscaluate the pressure drop values. Although both methods use the 2D particle injection assumption, it is interesting to note that at 6 mL and 8 mL, OpenFOAM underestimates the pressure drop values, whereas the resolved-unresolved CFD-DEM method overestimates the pressure drop values, and the difference is more profound at 8 mL. One possible explaination to this observation stems from the fact that, at 8 mL for example, the Case P2 which is based on the resolved-unresolved CFD-DEM method, shows that the filter is completely clogged with multiple layers of particles (along the vertical direction), whereas Case O2 which is obtained from OpenFOAM, shows that the entire filter (from top to bottom) is not com-

Case	P-y	O-y	E-y	P-x	O-x	E-x
1	40 mm	35 mm	40 mm	16 mm	18 mm	18 mm
2	40 mm	37 mm	40 mm	25 mm	30 mm	30 mm

Table 2 Particle distribution spread (y: vertical direction; x: horizontal direction). P = mixed resolved-unresolved CFD-DEM method; O = unresolved CFD-DEM method E = experimental data. Cases 1 and 2 are based on 4 mL and 8 mL solids volume respectively.

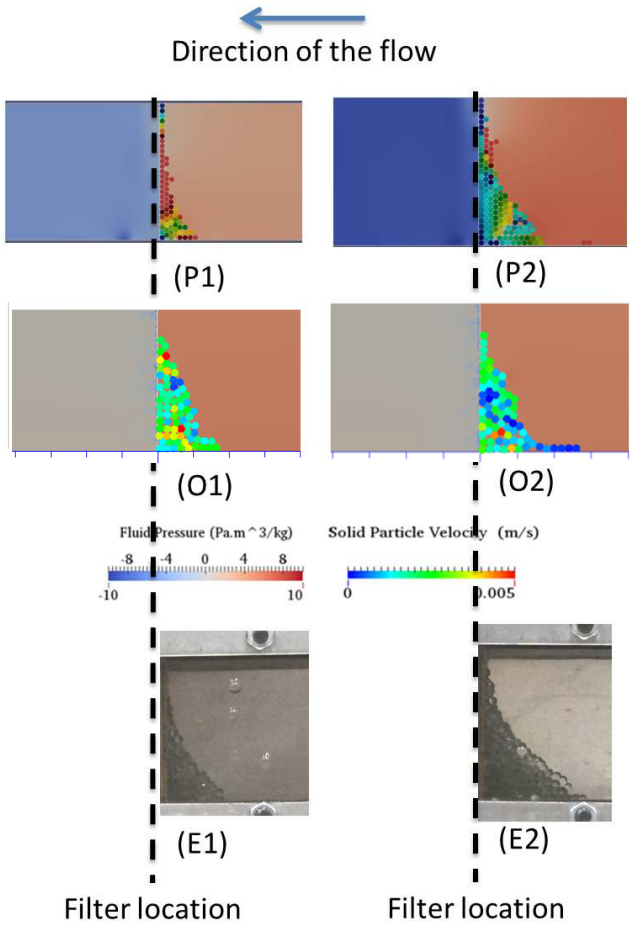

Fig. 6 Comparative Assessment between mixed resolved-unresolved CFD-DEM results (P1, P2), unresolved CFD-DEM results (O1, O2), and experimental results (E1, E2) based on three different solid volume (P1/O1/E1: 4 mL, P2/O2/E2: 8 mL)

pletely clogged with particles thereby explaining the lower pressure drop as compared to the mixed resolved-unresolved CFD-DEM method. The horizontal particle spread are very similar for all cases in both methods, as shown in Figure 6. There are several other reasons that may have played a role in the discrepancy between numerical and experimental pressure drop results. Firstly, for the mixed unresolved-resolved CFD-DEM method, the introduction of the MLS scheme (Section 3.1.3) may have led to pressure drop discrepancy; as such, rigorous

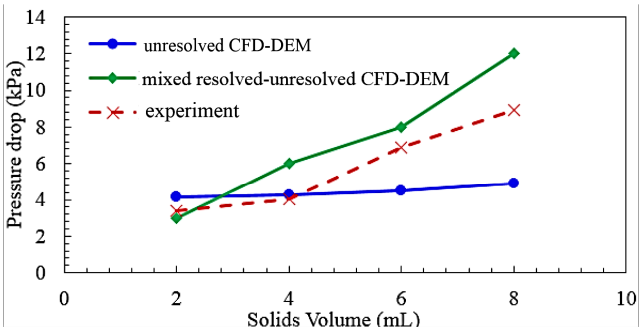

Fig. 7 Comparison between mixed resolved-unresolved CFD-DEM, unresolved CFD-DEM, and experimental pressure drop values

validation of the MLS scheme is to be conducted in the near future. Secondly, it is noted that the main limitation of the unresolved CFD-DEM approach is the grid size to particle diameter ratio. An extremely fine grid cannot be used for this method as this will lead to numerical stability issues. But without the use of very fine grids means that the fluid is not fully resolved in the vicinity of the particles thereby linking to the pressure drop discrepancy. Thirdly, further developments to the experimental setup for the purposes of obtaining more accurate quantitative experimental results is necessary. The interphase solid-liquid drag laws for both numerical methods requires further validation. Although both methods have some problems replicating certain cases, the numerical methods, overall, are capable of reproducing the experients relatively well especially the particle spread distribution patterns. The authors must reiterate that multiphase solid-liquid flows are prevalent in many environmental and engineering applications. However, the existing literature has extremely limited studies on modelling multiphase solid-liquid flows, especially with the use of the mixed unresolved-resolved CFD-DEM method, because accurately modelling these flows at different solid-gas scales of the problem is notoriously difficult. However, the methods and results presented in this paper will serve as a basis for further expanding the development of advanced (fully resolved) numerical methods and strategies for computational multiphase flows.

5 Conclusions and Perspectives

This study investigates the transient evolution of particle-laden liquid flow and particle accumulation on a filter by comparing the methodology and results of the CFD-DEM methodology developed in OpenFOAM and the mixed resolved-unresolved CFD-DEM technique. The results obtained by both numerical methods are then compared against experimental results. The numerical results comprising the pressure drop, particle accumulation, and particle distribution spread are in a resonable good agreement with the experimental results with the exception of higher solids volume. At higher solids volume, the pressure drop based on both numerical methods show deviation from the experimental data which is arguably due to the fact that the tightly packed particle deposits is not always in a rigid and tightly packed formation, among other root causes. However, the overall particle distribution patterns are in good agreement with the experimental results.

Interestingly, many studies including this study here are based on engineering applications where granular media (i.e. particle-fluid flows) is either dense or dilute. However, certain applications may have regions of dilute or dense flows. As such, it may not be practical to use the DEM throughout the entire domain, rather, DPM could be used. In short, a CFD-DEM-DPM could be used to accurately and rapidly obtain the numerical solution (i.e. use DEM in areas of high particle (dense) concentrations and use DPM in areas of low particle (dilute) concentrations. This could be achieved by a straightforward algorithm which assigns which particle solver to use, DEM or DPM, depending on the porosity of the CFD mesh cell. The next phase of this project comprises the implementation of the energy equation to account for thermal transport between solid particles and fluid continuum in the two numerical approaches. The next phase is to conduct 3D numerical simulations. This will be achieved after the development and implementation of MPI parallezation to deal with the performance bottleneck.

Compliance with Ethical Standards:

Conflict of Interest: On behalf of all authors, the corresponding author states that there is no conflict of interest.

The authors states there were no human participants or animals involved in this research project.

References

1. (1999) Petroleum project fact sheet fouling minimization, technical report
2. (2010) European aviation safety agency certification specification for engines cs-e, amendment 3 10
3. Baena S, Lawson C, Lam J (2012) Cold fuel test rig to investigate ice accretion on different pump inlet filter-mesh screens. In: 28th International Congress of the Aeronautical Sciences, ICAS
4. Balay S, Abhyankar S, Adams MF, Brown J, Brune P, Buschelman K, Dalcin L, Eijkhout V, Gropp WD, Kaushik D, Knepley MG, McInnes LC, Rupp K, Smith BF, Zampini S, Zhang H, Zhang H (2017) PETSc Web page. Http://www.mcs.anl.gov/petsc
5. Bayomy A, Saghir M, Yousefi T (2016) Electronic cooling using water flow in aluminum metal foam heat sink: Experimental and numerical approach. International Journal of Thermal Sciences 109:182–200
6. Caretto L, Gosman A, Patankar S, Spalding D (1972) Two calculation procedures for steady three-dimensional flows with recirculation. Proceedings of the Third International Conference on Numerical Methods in Fluid Mechanics 19:60–68
7. Cueto-Felgueroso L, Colominas I, Nogueira X, Navarrina F, Casteleiro M (2007) Finite volume solvers and moving least-squares approximations for the compressible navier–stokes equations on unstructured grids. Computer Methods in Applied Mechanics and Engineering 196:4712–4736
8. Cundall PA, Strack OD (1979) A discrete numerical model for granular assemblies. Geotechnique 29(1):47–65
9. De Bellis F, LA C (2012) Cfd optimization of an immersed particle heat exchanger. Applied Energy 97:841–848
10. Di Felice R (1994) The voidage function for fluid-particle interaction systems. International Journal of Multiphase Flow 20(1):153–159
11. Du Plessis JP, Masliyah JH (1991) Flow through isotropic granular porous media. Transport in Porous Media 6(3):207–221
12. Ebrahimi M, Crapper M, Ooi JY (2016) Numerical and experimental study of horizontal pneumatic transportation of spherical and low-aspect-ratio cylindrical particles. Powder Technology 293:48–59
13. Elghobashi S (1994) On predicting particle-laden turbulent flows. Applied Scientific Research 52(4):309–329
14. Feng Y, Yu A (2010) Effect of bed thickness on the segregation behavior of particle mixtures in a gas fluidized bed. Industrial & Engineering Chemistry

Research 49(7):3459–3468
15. Ferziger JH, Peric M (2012) Computational methods for fluid dynamics. Springer Science & Business Media
16. Geng Y, Che D (2011) An extended dem–cfd model for char combustion in a bubbling fluidized bed combustor of inert sand. Chemical Engineering Science 66(2):207–219
17. Gidaspow D (1994) Multiphase flow and fluidization: continuum and kinetic theory descriptions. Academic press
18. Goldschmidt M, Beetstra R, Kuipers J (2004) Hydrodynamic modelling of dense gas-fluidised beds: comparison and validation of 3d discrete particle and continuum models. Powder Technology 142(1):23–47
19. Gu L, Min J, Wu X, Yang L (2017) Airside heat transfer and pressure loss characteristics of bare and finned tube heat exchangers used for aero engine cooling considering variable air properties. International Journal of Heat and Mass Transfer 108:1839–1849
20. Jasak H (1996) Error analysis and estimation for the finite volume method with applications to fluid flows, 1996. PhD thesis, Ph. D. Thesis, University of London Imperial College
21. Kloss C, Goniva C, Aichinger G, Pirker S (2009) Comprehensive dem-dpm-cfd simulations-model synthesis, experimental validation and scalability. In: Proceedings of the Seventh International Conference on CFD in the Minerals and Process Industries, CSIRO, Melbourne, Australia
22. Kloss C, Goniva C, Hager A, Amberger S, Pirker S (2012) Models, algorithms and validation for open-source dem and cfd–dem. Progress in Computational Fluid Dynamics, an International Journal 12(2-3):140–152
23. Koch DL, Hill RJ (2001) Inertial effects in suspension and porous-media flows. Annual Review of Fluid Mechanics 33(1):619–647
24. Kubicki D, LO S (2012) Slurry transport in a pipeline–comparison of cfd and dem models. In: Ninth international conference on CFD in the minerals and process industries CSIRO, Melbourne, Australia
25. Kuruneru S, Sauret E, Saha S, Gu Y (2016) Numerical investigation of the temporal evolution of particulate fouling in metal foams for air-cooled heat exchangers. Applied Energy 184:531–547
26. Kuruneru S, Sauret E, Saha S, Gu Y (2017) A coupled finite volume and discrete element method to examine particulate foulant transport in metal foam heat exchangers. International Journal of Heat and Mass Transfer 115:43–61
27. Kuruneru S, Sauret E, Saha S, Gu Y (2018) Coupled cfd-dem simulation of oscillatory particle-laden fluid flow through a porous metal foam heat exchanger: Mitigation of particualte fouling. Chemical Engineering Science 179:32–52
28. Li L, Li B, Liu Z (2017) Modeling of spout-fluidized beds and investigation of drag closures using openfoam. Powder Technology 305:364–376
29. Liu G, Yu F, Lu H, Wang S, Liao P, Hao Z (2016) Cfd-dem simulation of liquid-solid fluidized bed with dynamic restitution coefficient. Powder Technology 304:186 – 197
30. Marchal E, Tomov P, Khelladi S, Bakir F (2014) A hybrid finite volume discrete elements for two-phase flows: application to snow showers in jet-engine fuel systems. In: IMA Conference on Mathematical Modelling of Fluid Systems
31. Marechal E (2016) Etude du colmatage des systèmes carburant de turboréacteurs par des suspensions denses de particules de glace. PhD thesis, Ecole Nationale Supérieure d'Arts et Métiers
32. Marshall J (2009) Discrete-element modeling of particulate aerosol flows. Journal of Computational Physics 228(5):1541–1561
33. Mezhericher M, Brosh T, Levy A (2011) Modeling of particle pneumatic conveying using dem and dpm methods. Particulate Science and Technology 29(2):197–208
34. Müller-Steinhagen H, Malayeri M, Watkinson A (2009) Heat exchanger fouling: environmental impacts. Heat Transfer Engineering 30(10-11):773–776
35. Müller-Steinhagen H, Malayeri M, Watkinson A (2011) Heat exchanger fouling: mitigation and cleaning strategies. Heat Transfer Engineering 32(3-4):189–196
36. Murray B, Broadley S, Morris G (2011) Supercooling of water droplets in jet aviation fuel. Fuel 90:433–435
37. OpenFOAM (2015) Relative tolerance openfoam userguide. http://www.openfoam.com/documentation/user-guide/fvSolution.php/
38. OpenFOAM (2016) Openfoam v4.1. https://openfoam.org/release/4-1/
39. OpenFOAM (2017) Openfoam v5 user guide: 4.5 solution and algorithm control. https://cfd.direct/openfoam/user-guide/fvsolution/
40. Pierre C, Bouyssier J, de Gournay F, Plouraboue F (2014) Numerical computation of 3d heat transfer in complex parallel heat exchangers using gen-

eralized graetz modes. Journal of Computational Physics 268:84–105
41. Piquet A, Roussel O, Hadjadj A (2016) A comparative study of brinkman penalization and direct-forcing immersed boundary methods for compressible viscous flows. Computers and Fluids 136:272–284
42. Qian F, Huang N, Lu J, Han Y (2014) Cfd-dem simulation of the filtration performance for fibrous media based on the mimic structure. Computers & Chemical Engineering 71:478–488
43. Ramgadia AG, Saha AK (2012) Fully developed flow and heat transfer characteristics in a wavy passage: Effect of amplitude of waviness and reynolds number. International Journal of Heat and Mass Transfer 55(9):2494–2509
44. Ramírez L, Nogueira X, Khelladi S, Chassaing J, Colominas I (2014) A new higher-order finite volume method based on moving least squares for the resolution of the incompressible navier-stokes equations on unstructured grids. Computer Methods in Applied Mechanics and Engineering 278:883–901
45. Reid M (2013) Engine fuel system tolerance to fuel born ice. managing water and ice in aviation fuel under low temperature conditions. In: Seminar proceedings
46. Rhie C, Chow W (1983) A numerical study of the turbulent flow past an isolated airfoil with trailing edge separation. AIAA Journal 21:1525–1532
47. Sleight P, Carter R (2008) Report on the accident to boeing 777-236er, g-ymmm, at london heathrow airport on 17 january 2008
48. Sturm M, Wirtz S, Scherer V, Denecke J (2010) Coupled dem-cfd simulation of pneumatically conveyed granular media. Chemical Engineering & Technology 33(7):1184–1192
49. Tian Z, Tu J, Yeoh G (2007) Numerical modelling and validation of gas-particle flow in an in-line tube bank. Computers & chemical engineering 31(9):1064–1072
50. Tryggvason G (2010) Virtual motion of real particles. Journal of Fluid Mechanics 650:1–4
51. Tsuji Y, Tanaka T, Ishida T (1992) Lagrangian numerical simulation of plug flow of cohesionless particles in a horizontal pipe. Powder technology 71(3):239–250
52. Tsuji Y, Kawaguchi T, Tanaka T (1993) Discrete particle simulation of two-dimensional fluidized bed. Powder technology 77(1):79–87
53. Wahyudi H, Chu K, Yu A (2016) 3d particle-scale modeling of gas–solids flow and heat transfer in fluidized beds with an immersed tube. International Journal of Heat and Mass Transfer 97:521–537
54. Wang FL, He YL, Tong ZX, Tang SZ (2017) Real-time fouling characteristics of a typical heat exchanger used in the waste heat recovery systems. International Journal of Heat and Mass Transfer 104:774–786
55. Wang S, Guo S, Gao J, Lan X, Dong Q, Li X (2012) Simulation of flow behavior of liquid and particles in a liquid–solid fluidized bed. Powder technology 224:365–373
56. Xiao H, Sun J (2011) Algorithms in a robust hybrid cfd-dem solver for particle-laden flows. Communications in Computational Physics 9(02):297–323
57. Xu J, Liu X, Pang M (2016) Numerical and experimental studies on transport properties of powder ejector based on double venturi effect. Vacuum 134:92–98
58. Yu A (2005) Powder processing models and simulations. In: Bassani, F.,Liedl, G.L., Wyder, P. (Eds.), vol 4. Encyclopedia of Condensed Matter Physics,invited contribution
59. Zhu H, Zhou Z, Yang R, Yu A (2007) Discrete particle simulation of particulate systems: theoretical developments. Chemical Engineering Science 62(13):3378–3396